



**HAL**  
open science

# Morphometrics and machine learning discrimination of the middle Eocene radiolarian species *Podocyrtis chalara*, *Podocyrtis goetheana* and their morphological intermediates

Francisco Pinto, Veronica Carlsson, Mathias Meunier, Bert Van Bocxlaer, Hammouda Elbez, Marie Cueille, Pierre Boulet, Taniel Danelian

## ► To cite this version:

Francisco Pinto, Veronica Carlsson, Mathias Meunier, Bert Van Bocxlaer, Hammouda Elbez, et al.. Morphometrics and machine learning discrimination of the middle Eocene radiolarian species *Podocyrtis chalara*, *Podocyrtis goetheana* and their morphological intermediates. *Marine Micropaleontology*, inPress, pp.102293. 10.1016/j.marmicro.2023.102293 . hal-04215322

**HAL Id: hal-04215322**

**<https://hal.science/hal-04215322>**

Submitted on 22 Sep 2023

**HAL** is a multi-disciplinary open access archive for the deposit and dissemination of scientific research documents, whether they are published or not. The documents may come from teaching and research institutions in France or abroad, or from public or private research centers.

L'archive ouverte pluridisciplinaire **HAL**, est destinée au dépôt et à la diffusion de documents scientifiques de niveau recherche, publiés ou non, émanant des établissements d'enseignement et de recherche français ou étrangers, des laboratoires publics ou privés.

1 **Morphometrics and machine learning discrimination of the middle Eocene radiolarian**  
2 **species *Podocyrthis chalara*, *Podocyrthis goetheana* and their morphological intermediates**

3

4 Francisco Pinto<sup>1</sup>, Veronica Carlsson<sup>1, 2</sup> \*, Mathias Meunier<sup>1</sup>, Bert Van Bocxlaer<sup>1</sup>, Hammouda  
5 Elbez<sup>2</sup>, Marie Cueille<sup>1</sup>, Pierre Boulet<sup>2</sup> and Taniel Danelian<sup>1</sup>

6 <sup>1</sup>Univ. Lille, CNRS, UMR 8198, Evo-Eco-Paleo, F-59000 Lille, France.

7 <sup>2</sup>Univ. Lille, CNRS, CRISAL – Centre de Recherche en Informatique Signal et Automatique  
8 de Lille, UMR 9189, F-59000 Lille, France.

9

10 **\*corresponding author: veronica.carlsson@univ-lille.fr**

11

12

13

14

15

16

17

18

19

20

21

22        **Abstract**

23        We present various approaches to distinguish the middle Eocene species *Podocyrtilis*  
24 *chalara* and *Podocyrtilis goetheana*, which are end members of a trajectory of phenotypic  
25 change, and their intermediate morphogroups. We constructed a set of thirteen traditional  
26 morphological variables to classify the entire morphological variability encompassed by the  
27 two morphospecies and their intermediates *Podocyrtilis* sp. cf. *P. chalara* and *Podocyrtilis* sp.  
28 cf. *P. goetheana*. We used two methods of classification, namely Linear Discriminant  
29 Analysis (LDA) and machine learning using artificial neural networks. LDA performed on the  
30 morphometric data reveals a good discrimination for *P. chalara*, *P. goetheana* and *Podocyrtilis*  
31 sp. cf. *P. goetheana*, but not for *Podocyrtilis* sp. cf. *P. chalara*. We used three approaches of  
32 machine learning based on different neural networks: Convolutional Neural Networks  
33 (CNNs) and two Spiking Neural Networks (SNNs). Each of these neural networks was trained  
34 based on classified images of the two morphospecies and their morphological intermediates,  
35 thus constituting a different set of input data than the morphometric dataset for LDA. The  
36 neural network approaches identified the same three morphospecies recognized by LDA from  
37 a dataset of traditional measurements, i.e. *P. chalara*, *P. goetheana* and *Podocyrtilis* sp. cf. *P.*  
38 *goetheana*, with up to 92 % accuracy. Our results highlight the great potential and promising  
39 perspectives of machine learning and neural networks in the application of image-based  
40 object recognition for morphological classification, which may also contribute to more  
41 objective taxonomic decisions.

42        **Keywords**

43        Morphometrics; Artificial Intelligence; Convolutional Neural Networks; Spiking Neural  
44        Networks; Radiolarians; Automated identification

45

## 46 **1. Introduction**

47 Polycystine radiolaria are one of the oldest known Rhizarian lineages, with a fossil  
48 record stretching back to the Early Cambrian (Obut and Iwata, 2000; Pouille et al., 2011) and  
49 is thus of much interest for a number of evolutionary studies (e.g., Danelian and Johnson,  
50 2001, Danelian et al., 2014, Renaudie and Lazarus, 2003, Tetard et al., 2017).

51 Since the early stages of the Deep Sea Drilling Program, the Cenozoic record of  
52 polycystine radiolaria has allowed us to establish their evolutionary and biostratigraphic  
53 significance, especially based on representatives of the Eocene genus *Podocyrtis*. (Sanfilippo  
54 and Riedel, 1970; Riedel, 1971; Moore, 1972; Riedel and Sanfilippo, 1978). Calibrated  
55 initially to the magnetostratigraphic time scale (Sanfilippo and Nigrini, 1998), the middle  
56 Eocene tropical radiolarian zones are now tied to orbital chronology (Meunier and Danelian,  
57 20222), which provides the highest resolution of temporal control possible today and allows  
58 to define biostratigraphic events more accurately. Indeed, many of the middle Eocene  
59 biozones are based on the evolution of the various lineages of the genus *Podocyrtis*, which  
60 often relate to gradual anagenetic changes in phenotypes, as documented in several  
61 evolutionary lineages since the early 1970s (Sanfilippo and Riedel 1970, 1992; Riedel, 1971).  
62 For example, the bases of biozones RP14 and RP15 are defined based on anagenetic  
63 phenotypic changes between the morphospecies *P. sinuosa* - *P. mitra* and *P. mitra* - *P.*  
64 *chalara*, respectively.

65 The *Podocyrtis (Lampterium)* lineage ends with the marked morphological transition  
66 of *Podocyrtis chalara* to *P. goetheana*. Interestingly, the first occurrence of *P. goetheana*  
67 defines the base of biozone RP16 (Sanfilippo and Nigrini, 1998); an anagenetic transition was  
68 reported, but intermediate forms were never documented in detail. The absence of such a  
69 documentation has implications for our understanding of evolutionary changes in this  
70 *Podocyrtis* lineage, but as intermediate forms are poorly understood it also affects the

71 recognition of the base of RP16. Here we examine the well-preserved radiolarian material of  
72 ODP Sites 1259 and 1260 from Demerara Rise (equatorial Atlantic Ocean), which present an  
73 exceptionally expanded Eocene sedimentary sequence. As such, this material offers an  
74 exceptional opportunity to study the morphological transitional forms between *P. chalara* and  
75 *P. goetheana*.

76         Within the abovementioned context, the principal aim of our study is to document  
77 morphological variation in the anagenetic sequence of *P. chalara* to *P. goetheana* with two  
78 different but complementary approaches to test the performance of various machine learning  
79 algorithms based on neural networks. To reach this objective, we first quantified  
80 morphological variation in the anagenetic transition between *P. chalara* and *P. goetheana*  
81 with traditional morphometrics, i.e., linear measurements, pore counts and associated ratios in  
82 the framework of qualitatively recognized morphological entities. This quantification of shape  
83 follows previous attempts to assess morphological changes in the *Podocyrtes (Lampterium)*  
84 lineage (Sanfilippo and Riedel, 1990; Rohlf and Bookstein, 1991; Danelian and Macleod,  
85 2019; Watanabe et al., 2022). Using this morphometric framework of measurement data and *a*  
86 *priori* morphospecies assignments, we examined how well linear discriminant analysis allows  
87 to distinguish morphospecies as a baseline to test the performance of machine learning with  
88 neural networks.

89         Testing the capabilities of neural network approaches based on image recognition is a  
90 daunting task, because during the past couple of years, a variety of techniques involving  
91 Artificial Neural Networks (ANNs) have been developed and improved. Convolutional  
92 Neural Networks (CNNs) have been specifically designed for analysis of visual data, and are  
93 now commonly used for image recognition, warranting detailed examinations of their  
94 performance in morphological classification, and, therewith, as a tool to inform, and  
95 potentially reach more objective taxonomic decisions. Indeed, CNNs are becoming well-

96 integrated in various micropaleontological studies for automatic image recognition (i.e., Mitra  
97 et al., 2019, Hsiang et al., 2019; Marchant et al., 2020; Dollfus and Beaufort, 1999; Beaufort  
98 and Dollfus, 2004; Bourel et al., 2020; Itaki et al., 2020; Renaudie et al., 2018; Tetard et al.,  
99 2020). Regarding Eocene radiolaria, a recent study by Carlsson et al. (2022) applied a CNN to  
100 eight well-delimited morphospecies of the genus *Podocyrthis*, and documented the potential of  
101 this method under the simplified scenario when no morphological intermediates are present.  
102 Spiking Neural Networks (SNNs) present another type of neural network, which in addition to  
103 neuronal and synaptic states, they also incorporate a time component; this is why such  
104 networks can more closely mimic natural neural networks (Maass, 1997). SNNs have wide  
105 applicability, including modeling of natural systems such as the central nervous system of  
106 biological organisms, as well as for image analysis. Traditionally, SNNs were less accurate  
107 than other neural networks, but in recent years their performance has significantly improved;  
108 they are more appropriate to process spatio-temporal data, and they may use computational  
109 resources more effectively (Tavanaej et al., 2019). As such, an evaluation of SNNs in image  
110 recognition and biological classification seems warranted.

111 In this paper, we expand on previous work by Carlsson et al (2022) with CNNs by  
112 aiming to classify stacked and segmented images of the entire spectrum of morphological  
113 variation found between *P. chalara* and *P. goetheana*. As mentioned, we used morphometrics  
114 to document shape variability, which we subjected together with *a priori* morphospecies  
115 assignments to LDA as a baseline to study the classification performance for image-based  
116 neural networks using a CNN, a Spike-timing-dependent plasticity (STDP)-based SNN and a  
117 SuperSpike-based SNN. This examination allows us to evaluate the use of imaging data and  
118 neural networks for automated classification in a complex case study with intermediate  
119 shapes. If the neural networks perform well, we would expect correct classification for each  
120 morphogroup. Additionally, the results should reflect those of the LDA analysis, if the

121 morphometric documentation of shape variation is representative of the four morphospecies.  
122 Alternatively, neural networks may show differences compared to LDA. These distinctions  
123 could arise if neural networks fail to perform well, possibly due to unsuccessful training with  
124 the existing data. In opposite to that, the neural networks may perform better than LDA if the  
125 data supporting LDA lacks crucial shape information necessary for distinguishing between  
126 morphogroups based on the images. As such, we expect our study to shed light into future  
127 opportunities for automated biological classification of polycystine radiolaria and the use of  
128 neural networks in developing more objective taxonomic decisions.

129

## 130 **2. Analyzed morphological groups**

131 Plate 1 displays the entire range of morphological variability observed between *P. chalara*  
132 and *P. goetheana*. As linear discriminant analysis and the supervised learning of neural  
133 networks are based on *a priori* group assignments, we were required to assign this continuum  
134 of variation to a number of morphological groups. Based on extensive qualitative assessments  
135 and to challenge the employed classification algorithms we recognized four distinct  
136 morphological groups for the purpose of the current study, without currently being concerned  
137 by the paleobiological/evolutionary status of each group. These morphogroups are briefly  
138 presented below.

139

140 *Podocyrtes chalara* Riedel and Sanfilippo

141 [Pl. 1, fig. A, B](#)

142 1970 *Podocyrtes (Lampterium) chalara* Riedel and Sanfilippo, p. 535, pl. 12, figs. 2, 3.

143 1971 *Podocyrtes (Lampterium) chalara* Riedel and Sanfilippo: Moore, p. 743, pl. 3, figs. 5,

144 6.

- 145 1972 *Lampterium chalara* Riedel and Sanfilippo: Petrushevskaya and Kozlova, p. 543, pl.  
146 32, fig. 12.
- 147 1978 *Podocyrtis (Lampterium) chalara* (Riedel and Sanfilippo): Riedel and Sanfilippo, p.  
148 71, pl. 8, fig. 3, text-fig. 3.
- 149 2012 *Podocyrtis (Lampterium) chalara* Riedel and Sanfilippo: Kamikuri, p. 103, pl. 3, figs.  
150 2a, 2b.
- 151 2012 *Podocyrtis (Lampterium) chalara* Riedel and Sanfilippo: Moore and Kamikuri, p. 9,  
152 pl. P7, fig. 8.

153

154 Distinguishing characters: We include here forms displaying twelve or less vertically well-  
155 aligned, subangular abdominal pores of similar size per horizontal row, illustrating the classic  
156 morphology of *P. chalara*. Specimens of this morphogroup display less than thirteen pores on  
157 the circumference of the abdomen.

158

159 *Podocyrtis* sp. cf. *P. chalara* Riedel and Sanfilippo

160 [Pl. 1](#), fig. C, D

161 1972 *Lampterium* sp. G: Petrushevskaya and Kozlova, pl. 32, fig. 10.

162 1972 *Lampterium* sp. aff. *L. goetheana*: Petrushevskaya and Kozlova, pl. 32, fig. 13.

163 2022 *Podocyrtis (Lampterium) chalara* Riedel and Sanfilippo: Meunier and Danelian, p. 21,  
164 pl. 2.4.

165

166 Distinguishing characters: This morphogroup includes specimens that have a similar outline  
167 and appearance as *P. chalara*, but they display vertically misaligned subangular abdominal  
168 pores of different size. Specimens of this morphogroup may display vertical rows of pores  
169 that are shifted to the right or left compared to the rows of pores above and below, giving a



170 twisted appearance for the rows of pores developed on the abdomen, with result a  
171 honeycomb-like pore pattern. These shifts may be so extensive that the arrangement of pores  
172 on the abdomen becomes chaotic, preventing the possibility to trace any apparent abdominal  
173 rows or vertical alignment.

174

175 *Podocyrtis* sp. cf. *P. goetheana* (Haeckel)

176 [Pl. 1](#), figs. E - L

177 2006 *Podocyrtis (Lampterium) chalara* Riedel and Sanfilippo: Funakawa et al., p. 29, pl.  
178 P9, figs. 11a, 11b.

179

180 Distinguishing characters: This morphogroup is mainly characterized by an increase in total  
181 size, but with a significant reduction in the number of abdominal pores compared to both  
182 variants of *P. chalara*. It differs from *P. goetheana* in that the bars of the second row of  
183 abdominal pores are thicker and not always elongated, nor parallel to each other, as the  
184 formation of the honeycomb-like pattern of pores becomes more apparent. This morphogroup  
185 displays a high degree of morphological variability.

186

187 *Podocyrtis goetheana* (Haeckel)

188 [Pl. 1](#), figs. M - O

189 1887 *Cycladophora goetheana* Haeckel, p. 1376, pl. 65, fig. 5.

190 1970 *Podocyrtis (Lampterium) goetheana* (Haeckel): Riedel and Sanfilippo, p. 535.

191 1971 *Podocyrtis (Lampterium) goetheana* (Haeckel): Moore, p. 743, pl. 3, figs. 7, 8.

192 1972 *Lampterium* sp. aff. *L. goetheana* Petrushevskaya and Kozlova, pl. 32, fig. 14.

193 2005 *Podocyrtes (Lampterium) goetheana* (Haeckel): Nigrini et al., p. 45, pl. P5, figs. 11,  
194 12.

195 2006 *Podocyrtes (Lampterium) goetheana* (Haeckel): Funakawa et al., p. 29, pl. P9, figs.  
196 12a, 12b.

197 2012 *Podocyrtes (Lampterium) goetheana* (Haeckel): Kamikuri, p. 103, pl. 3, fig. 1.

198 2012 *Podocyrtes (Lampterium) goetheana* (Haeckel): Moore and Kamikuri, p. 9, pl. P7, fig.  
199 9.

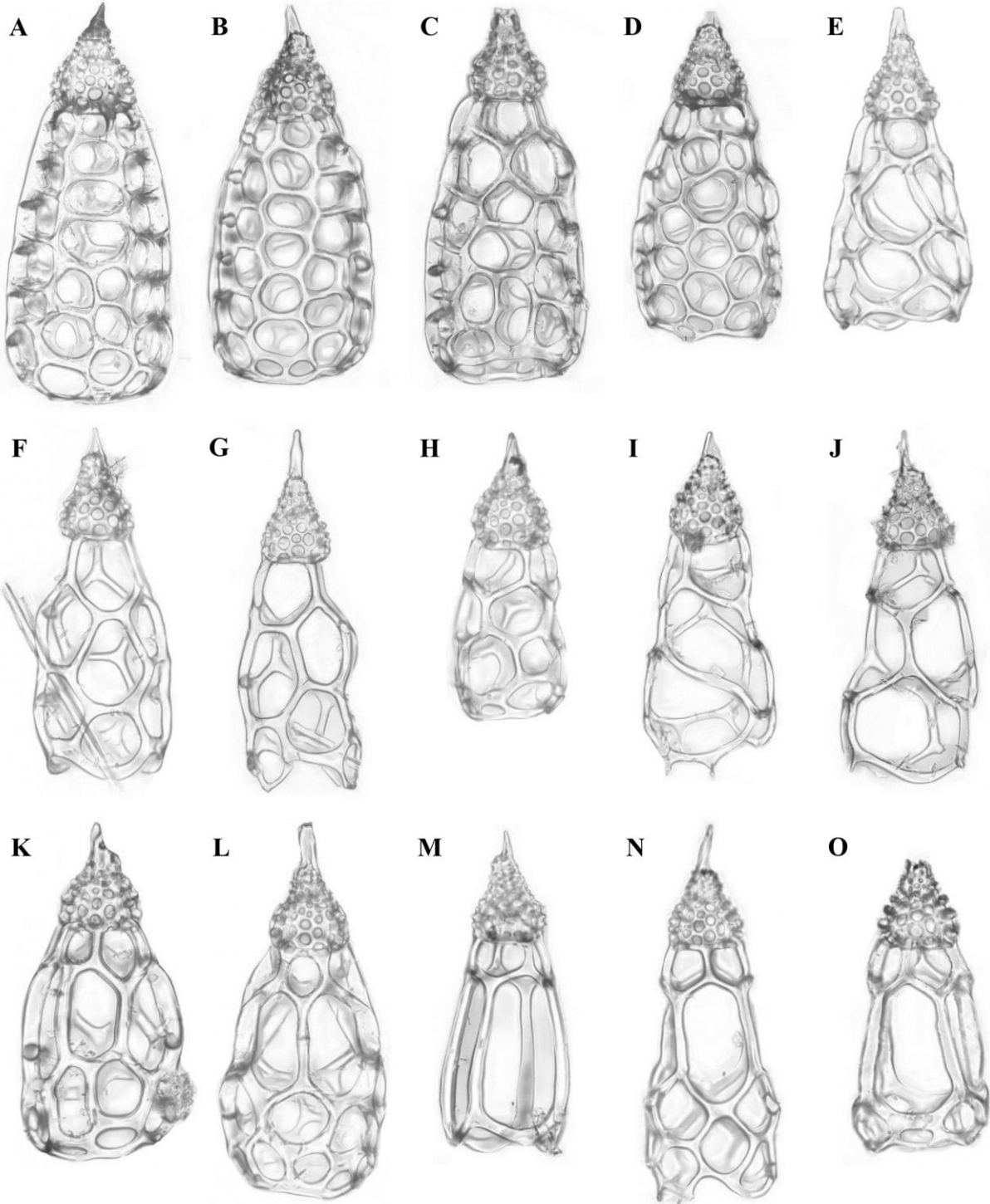
200 2022 *Podocyrtes (Lampterium) goetheana* (Haeckel): Meunier and Danelian, p. 21, pl. 2.5.

201

202 Distinguishing characters: This group includes only forms that display elongated straight bars  
203 formed at the level of the second horizontal row of pores on the abdomen. This feature is  
204 typical for *P. goetheana* as originally described, and, as mentioned above, the first occurrence  
205 of typical *P. goetheana* defines the base of the RP16 Zone.

206

207 **Plate 1.** Composite light micrographs of *Podocyrtes* radiolaria from ODP Site 1260, processed and scaled in  
208 ImageJ. (A) and (B) *Podocyrtes chalara*, samples: ODP 1260A-6R-5W, 63-65 cm and ODP 1260A-6R-5W, 20-  
209 22 cm; (C) and (D) *Podocyrtes* sp. cf. *P. chalara*, samples: ODP 1260A-6R-4W, 68-70 cm and ODP 1260A-6R-  
210 5W, 20-22 cm; (E) to (L) *Podocyrtes* sp. cf. *P. goetheana*, samples: ODP 1260A-6R-4W, 68-70 cm; ODP  
211 1260A-6R-5W, 15-17 cm and ODP 1260A-6R-5W, 87-89 cm; (M) to (O) *Podocyrtes goetheana*, sample: ODP  
212 1260A-6R-1W, 58-60 cm.



50µm

213

214

### 215 **3. Materials and methods**

#### 216 **3.1. Sediment samples**

217 The material analyzed in this study consists of radiolaria obtained from an expanded  
218 middle Eocene siliceous chalk sequence drilled at ODP Sites 1259 and 1260 (Leg 207,  
219 Demerara Rise), located in the equatorial region of the Atlantic Ocean, 380 km offshore  
220 Suriname (Erbacher et al., 2004; Danelian et al., 2005). The middle Eocene sequence is  
221 particularly thick at Sites 1259 and 1260 and contains siliceous microfossils (radiolarians,  
222 diatoms) of an excellent state of preservation (Danelian et al., 2007; Renaudie et al., 2010;  
223 Meunier and Danelian, 2022, 2023). The part of the limestone sequence from Site 1260 that is  
224 studied here is dated by orbito-chronology (Westerhold and Röhl, 2013). More specifically,  
225 our samples span the interval between 41.24 Ma and 39.84 Ma. Site 1259 is dated via bio- and  
226 magneto-stratigraphy and was sampled in the interval between ~39.05 and 37.70 Ma.

227

#### 228 **3.2. Slide preparation**

229 A combined total of 15 samples from both sites were chosen and prepared for  
230 microscopic observation using techniques described by Sanfilippo et al. (1985). A small  
231 quantity (~2 cm<sup>3</sup>) of unprocessed sediment was collected from each sample and dried  
232 overnight at 50°C to eliminate any residual water. After being weighed, sediment samples  
233 were soaked for 2 hours in a 500 mL polypropylene beaker containing 30 mL of 30 %  
234 hydrochloric acid (HCl), to dissolve their carbonate content and concentrate siliceous  
235 microfossils. A few mL of HCl were added at the end to confirm the end of the reaction. The  
236 residues resulting from the acid treatment was then washed by adding ~200 mL of distilled  
237 water. After 2 hours of decantation, excess water was carefully removed using a pipette.  
238 Residues were subsequently soaked for 2 hours in 30 mL of 10 % hydrogen peroxide (H<sub>2</sub>O<sub>2</sub>)

239 to remove organic matter, and subsequently washed through a 63  $\mu\text{m}$  sieve using distilled  
240 water. The  $> 63 \mu\text{m}$  fraction was then exposed to ultrasonic waves for 10 min, then passed  
241 again through the 63  $\mu\text{m}$  sieve, and finally left to dry overnight at 50°C. For each sample, ~2  
242 g of dried residue was carefully spread on top of a slide covered with several drops of Norland  
243 Optical Adhesive 61, then topped with a coverslip and sealed by two minutes of exposure to  
244 UV light.

245

### 246 **3.3. Microscopy and image processing**

247 The resulting slides were analyzed with a Zeiss AXIO Images A2 microscope under  
248 transmitted light at  $\times 10$  and  $\times 20$  magnifications. All specimens recognized qualitatively as *P.*  
249 *chalara*, *Podocyrtis* sp. cf. *P. chalara*, *Podocyrtis* sp. cf. *P. goetheana* or *P. goetheana* were  
250 manually photographed using the mounted Axiocam ERc5s with Zen 3.5 (blue edition)  
251 software. For each specimen, a batch of 5-10 photographs were taken at different focal points  
252 to obtain a series of images, which were stacked afterwards using Helicon Focus 7.7.0  
253 (HeliconSoft) to create a composite picture entirely in focus. The stacked images were  
254 subsequently retouched with Paint3D to facilitate their automated segmentation. This last  
255 procedure was performed with the ImageJ BioVoxxel plugin (Brocher, 2022) and the  
256 AutoRadio\_Segmenter plugin developed for ImageJ / Fiji (Tetard et al., 2020).

257

### 258 **3.4. Morphometric analyses**

259 As we aimed to subject specimens to discriminant analysis based on morphometric  
260 measurements, it was essential that the documented morphological variables would  
261 adequately capture shape variations present in between the four morphogroups. We first  
262 designed a set of variables that would allow to compare with the variables used by Watanabe

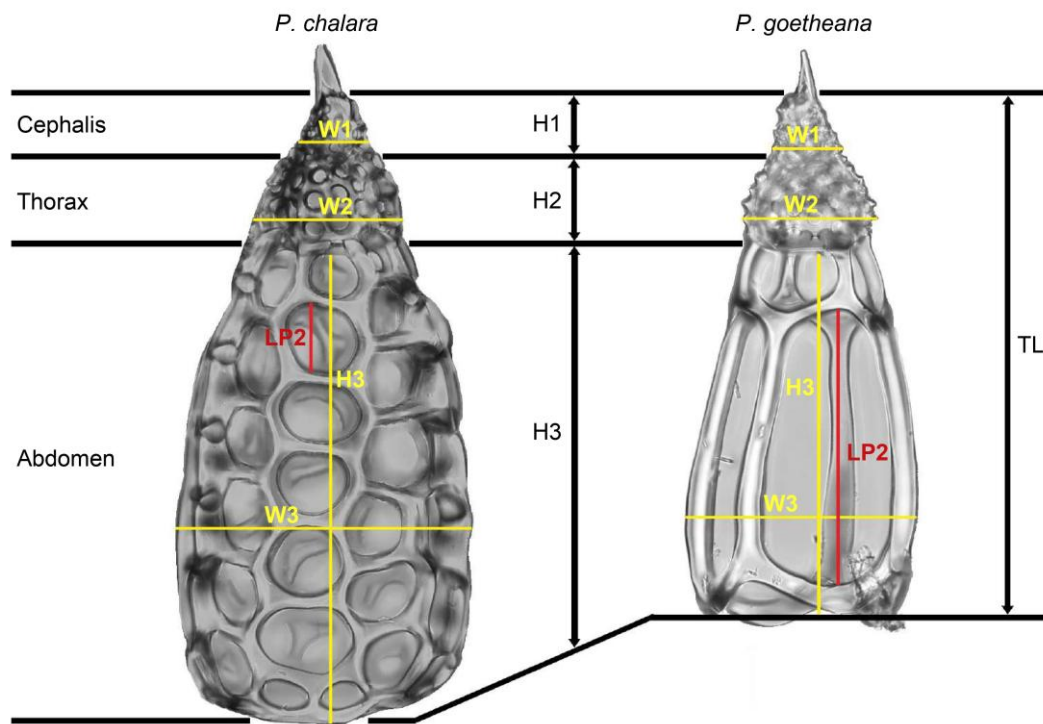
263 et al. (2022) on the specimens of the *Lampterium* lineage from the Pacific Ocean. A subset of  
264 seven of these variables was retained and supplemented with six newly proposed variables to  
265 result in a set of thirteen morphological variables that document well the morphological  
266 variation between the four morphogroups (Figure 1). The seven morphological variables  
267 proposed by Watanabe et al. (2022) are:

- 268 - W1: Maximal width of the cephalis
- 269 - W2: Maximal width of the thorax
- 270 - W3: Maximal width of the abdomen
- 271 - H1: Maximal height of the cephalis
- 272 - H2: Maximal height of the thorax
- 273 - H3: Maximal height of the abdomen
- 274 - TL: Total length or height of the specimen

275 and our six additional variables are:

- 276 - LP2: Maximum length of the second abdominal pore along along the axis used to  
277 measure H3 (with the first pore being the one closest to the thorax-abdomen border)
- 278 - NPV: Number of abdominal pores aligned vertically along the axis used to measure  
279 H3 (on the front-facing side of the skeleton)
- 280 - NPH: Number of abdominal pores aligned horizontally behind the axis of W3 (on the  
281 front-facing side of the skeleton)
- 282 - R1: Maximum length of the second pore of the abdomen / H3
- 283 - R2: Number of abdominal pores aligned vertically behind the axis of H3 / H3
- 284 - R3: Number of abdominal pores aligned horizontally behind the axis of W3 / W3

285



286

287 **Figure 1.** Schematic representation of the eight skeletal variables measured for all specimens outlined in Table  
 288 1. Five additional variables related to pore counts and ratios are not illustrated. Abbreviations: W1: maximum  
 289 width of the cephalis; W2: maximum width of the thorax; W3: maximum width of the abdomen; H1: maximum  
 290 height of the cephalis without the apical horn; H2: maximum height of the thorax; H3: maximum height of the  
 291 abdomen; TL: total length or height of the specimen without the apical horn; LP2: maximum length of the  
 292 second abdominal pore.

293

294 Quantifications of these variables (**Table S1** in **Supplementary materials**) were directly  
 295 performed on a dataset of 214 photographs/specimens from samples 1260A-6R-1W, 58-60  
 296 cm, 1260A-6R-4W, 68-70 cm, 1260A-6R-5W, 15-17 cm and 1260A-6R-5W, 87-89 cm,  
 297 outlined in **Table 1**, using the image processing and analysis software ImageJ (Schneider et  
 298 al., 2012). All of these data were tabulated and then imported in the statistical environment R  
 299 (v. 4.1.3; R Core Team 2022) for subsequent LDA using the packages MASS (v. 7.3-60;  
 300 Ripley et al., 2013) and vegan (v. 2.6-4; Oksanen et al., 2013). This analysis is a constrained

301 ordination procedure that uses a linear combination of coefficients to maximize the distance  
 302 between *a priori* defined groups, while minimizing the distance within each group (Venables  
 303 and Ripley, 2002). As morphometric variables were expressed in both metric units and as  
 304 ratios, the LDA was performed on data that were transformed to have the mean at zero- and  
 305 one-unit standard deviation (z transformation). After subjecting the whole dataset to LDA we  
 306 performed cross-validation by 100 replicates of randomly assigning 80 % of the data to a  
 307 training dataset and the remainder to a testing set to evaluate the classification success of the  
 308 LDA.

309

310 **Table 1.** Number of specimens analyzed per morphogroup and per sampled core interval.

Samples	<i>P. chalara</i>	<i>Podocyrctis</i> sp. cf. <i>P. chalara</i>	<i>Podocyrctis</i> sp. cf. <i>P. goetheana</i>	<i>P. goetheana</i>	Total number of measured specimens per sample
1260A 6R 1W 58-60cm	0	0	2	29	31
1260A 6R 4W 68-70cm	18	19	37	0	74
1260A 6R 5W 15-17cm	19	12	7	0	38
1260A 6R 5W 87-89 cm	34	9	28	0	71

311

312

### 313 **3.55. Artificial Neural Networks**

314 Artificial Neural Networks or simply neural networks are machine learning algorithms  
 315 designed to simulate the decision-making processes of the human brain by analyzing and  
 316 exploiting patterns in data (Yang and Yang, 2014). Prior to analysis, the data given to a  
 317 network is split into two parts, one for training and one for testing, usually in a 80 to 20 ratio.  
 318 The first set of data is used to train the neural network, so that to enable it to learn recognizing



319 features and patterns present in the data, whereas the second set of data is used to test the  
320 performance of the network to classify cases based on the previously trained capabilities of  
321 recognition.

322 A type of ANNs that has been specifically designed to analyze visual data are CNNs,  
323 commonly used for image recognition. They are designed to analyze visual data by  
324 considering the color values of each pixel and by identifying patterns within images (Hijazi et  
325 al., 2015). CNNs utilize a process known as convolution. Convolution can be described as a  
326 linear operation to decompose the input image by sliding small windows known as filters or  
327 kernels over the input image to construct layers that each obtain certain features. The  
328 convolutional layers in a CNN modify gradually the image parameters, such as weights or  
329 bias, to learn and recognize specific patterns or objects in the images. By adjusting these  
330 parameters through training, the network aims to correctly classify the output given a  
331 particular input. When a CNN has multiple layers, typically more than three, the procedure is  
332 referred to as deep learning, as each layer enables the recognition of more and more advanced  
333 features in an image. As mentioned, SNNs consider additionally the time factor, alike  
334 biological neurons, which use discrete spikes to compute and transmit information, instead of  
335 characterizing neurons by a single, static continuous-valued activation.

336 The hyperparameters (i.e. weights) of the neural network analyzed in this study were  
337 chosen randomly; more specifically a value between -1 and 1 was chosen for the VGG16 and  
338 SuperSpike-based networks, while a value network between 0 and 1 was chosen for the  
339 STDP-based network neural. We analyzed two sets of stacked and segmented images. The  
340 first set contained images with *a priori* assignments to the four morphogroups represented in  
341 section 2; for the second set assignments were altered based on the results of LDA. In each  
342 case, we performed ten runs per type of neural network used, with 20 epochs for each  
343 network, except for the STDP-based network that was run with 100 epochs. An epoch simply

344 means how many passes it goes through the training set and updates parameters based on each  
345 pass. The following neural networks were used to perform runs:

346 - Visual Geometry Group 16 (VGG16). This 16-layer deep CNN was used for its  
347 simplicity. For our analyses, we use transfer learning, meaning that the first 15 layers  
348 were already pre-trained based on a large-scale image dataset from ImageNet, and we  
349 only trained the last layer specifically using our data and PyTorch (Paszke et al.,  
350 2019). More information about VGG16 is provided by Simonyan and Zisserman  
351 (2015).

352 - STDP-based Spiking Neural Network (STDP-Network). This network contains  
353 convolutional and pooling layers that learn the features from the data using a Spike  
354 Timing Dependent Plasticity (STDP), a learning algorithm inspired by natural  
355 neurons. STDP adapts the synaptic connections between the neurons based on the  
356 timing of the spikes to transmit information (Masquelier and Thorpe, 2007) in an  
357 unsupervised way, i.e., without *a priori* group assignments. This SNN is then  
358 combined with a Support Vector Machine (SVM) for classification in the STDP-based  
359 network using the *a priori* group assignments (Cortes and Vapnik, 1995). To train the  
360 STDP-Network, we used the CSNN-simulator (Falez, 2019).

361 - SuperSpike-based Spiking Neural Network (SuperSpike-Network). This SNN is  
362 trained using a nonlinear voltage-based three-factor learning rule capable of training  
363 multilayer networks called the SuperSpike (Zenke and Ganguli, 2018), which is a  
364 supervised global learning rule similar to deep learning. We used the Norse simulator  
365 for our analyses (Pehle and Pedersen, 2021).

366

367 All the neural network simulations were conducted on the cluster “grouille” of the Grid’5000  
368 test bed (Balouek et al., 2013) using two Nvidia A100-PCIE-40GB GPUs, an AMD EPYC

369 7452 32 core CPU (Zen 2, 2 CPUs/node), and 128GB of RAM. For each type of neural  
 370 network, we averaged the assignment accuracies obtained over the ten replicate runs to gain  
 371 robust insight into performance.

372 The training of the neural networks are expected to be better when a large, data-rich training  
 373 set is used. Because our two analyzed datasets (Tables 2 and 3) are composed of 428 and 514  
 374 original images, respectively, we considered it necessary to augment the data available for  
 375 ANN training. Therefore, we performed the following data augmentation procedures:

- 376 — Rotate the images by a randomized angle between -15 and 15 degrees and keep all copies.
- 377 — Randomly choose images that would be flipped from left to right and keep both copies.
- 378 — Rescale random images with values between 1 and 1.3 (with 1 being the default scale  
 379 value).

380 The total number of images in each dataset was enhanced to >1000 images via data  
 381 augmentation.

382

**Table 2.** List of images included (prior to augmentation) in each of the classes for the four- class dataset used for analysis withVGG16with.

Samples	<i>P. chalara</i>	<i>Podocyrtis</i> sp. cf. <i>P. chalara</i>	<i>Podocyrtis</i> sp. cf. <i>P. goetheana</i>	<i>P. goetheana</i>	Total number of analyzed specimens per sample
1260A 6R 4W 68-70cm	0	19	34	3	56
1260A 6R 4W 119-121cm	0	13	2	1	16
1260A 6R 5W 15-17cm	0	12	7	0	19
1260A 6R 5W 63-65cm	22	9	15	0	46
1260A 6R 5W 87-89 cm	33	12	18	14	77
1260A 6R 6W 20-22 cm	12	18	9	0	39
1260A 6R 6W 57-59 cm	19	14	2	0	35
1260A 7R 1W 22-24 cm	24	15	0	0	39
1260A 7R 1W 69-71 cm	33	11	0	0	44

1260A 7R 1W 121-123 cm	31	11	0	0	42
1260A 7R 2W 19-21 cm	0	13	0	0	13
1260A 8R 3W 65-67cm	0	1	0	0	1
<b>TOTAL</b>	<b>174</b>	<b>148</b>	<b>87</b>	<b>18</b>	<b>427</b>

**Table 3.** List of images included (prior to augmentation) in each of the classes for the three class three dataset used for analysis with VGG16, STDP- based SNN and SuperSpike-based SNN.

Samples	<i>P. chalara</i> + <i>Podocyrstis</i> sp. cf. <i>P. chalara</i>	<i>Podocyrstis</i> sp. cf. <i>P. goetheana</i>	<i>P. goetheana</i>	Total number of analyzed specimens per sample
1259A 17R 1W 54-56cm	0	0	1	1
1259A 18R 1W 53-55cm	0	0	41	41
1259A 18R 2W 53-55cm	0	0	36	36
1260A 6R 1W 58-60cm	0	1	26	27
1260A 6R 4W 68-70cm	19	29	0	48
1260A 6R 4W 119- 121cm	13	2	1	16
1260A 6R 5W 15-17cm	12	5	0	17
1260A 6R 5W 63-65cm	31	15	0	46
1260A 6R 5W 87-89cm	43	28	0	71
1260A 6R 6W 20-22cm	29	8	0	37
1260A 6R 6W 57-59cm	34	2	0	36
1260A 7R 1W 22-24cm	39	0	0	39
1260A 7R 1W 69-71cm	44	0	0	44
1260A 7R 1W 121- 123cm	42	0	0	42
1260A 7R 2W 19-21cm	13	0	0	13
<b>TOTAL</b>	<b>319</b>	<b>90</b>	<b>105</b>	<b>514</b>

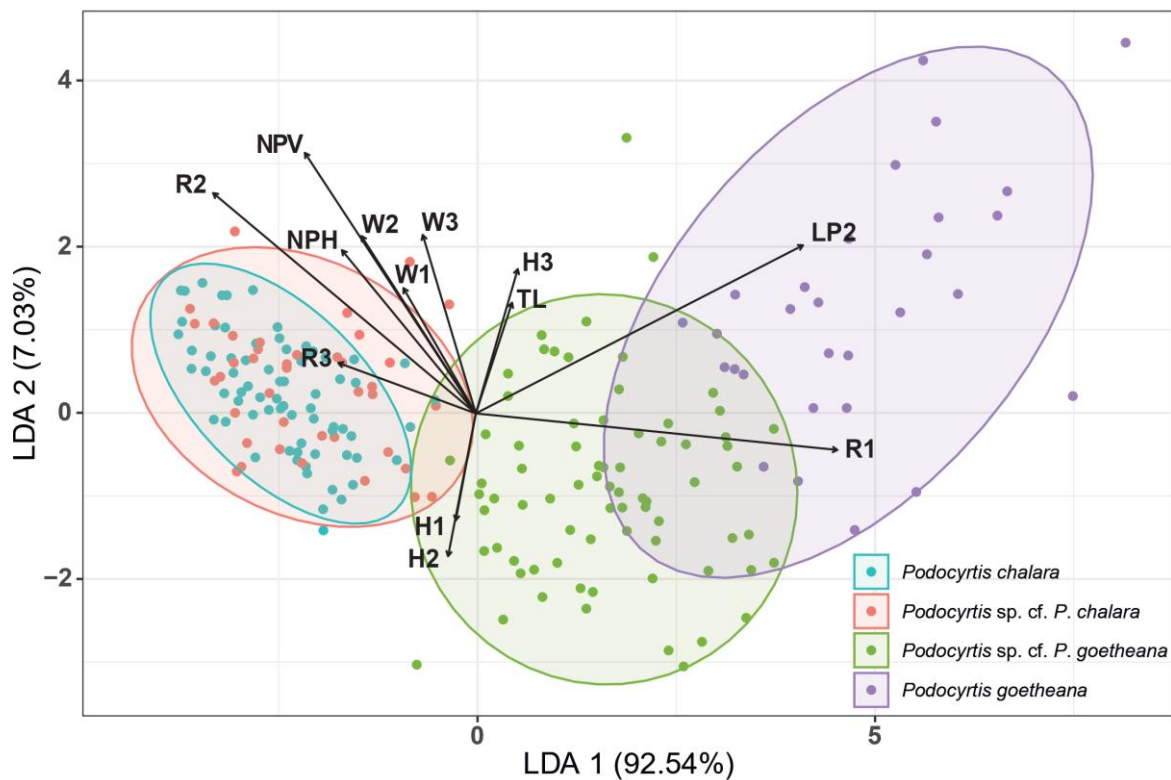
383

## 384 4. Results

### 385 4.1. Morphometrics and linear discriminant analysis

386 The LDA performed on the matrix of our 13 morphometric variables, i.e., measurements, pore  
387 counts and ratios, represented >99 % of the variation on the first two axes and clustered  
388 *Podocyrstis goetheana* and *Podocyrstis* sp. cf. *P. goetheana* successfully (Fig. 2).  
389 Comparatively, specimens belonging to *P. chalara* were regularly confused with *Podocyrstis*

390 sp. cf. *P. chalara* and vice versa, resulting overall in  $73.5 \pm 6.1$  % (mean  $\pm$  sd) correct  
 391 assignments (Table 4). These two latter morphogroups overlap completely on the LDA plot,  
 392 whereas *P. Podocyrtis* sp. cf. *P. goetheana* and *P. goetheana* are relatively well-separated  
 393 from *P. chalara* and *Podocyrtis* sp. cf. *P. chalara*, although they share limited overlap with  
 394 each other (Figure 2). The first axis of the LDA mainly represents size variations of the  
 395 second row of abdominal pores. The morphological variables that contribute the most to  
 396 discriminate the morphogroups on the first LDA axis correspond to the maximum length of  
 397 the second abdominal pore (LP2), and the maximum length of the second pore of the  
 398 abdomen/maximum height of the abdomen (R1).



399  
 400 **Figure 2.** Scatter plot of the two first axes of the Linear Discriminant Analysis (LDA) conducted on the 13  
 401 variables that constituted the morphometric data using four *a priori* identified morphogroups (indicated in the  
 402 legend; ellipses correspond to the 95 % confidence intervals for each morphogroup). Abbreviations: W1:  
 403 maximum width of the cephalis without the apical horn; W2: maximum width of the thorax; W3: maximum  
 404 width of the abdomen; H1: maximum height of the cephalis; H2: maximum height of the thorax; H3: maximum  
 405 height of the abdomen; TL: total length or height of the specimen without the apical horn; LP2: maximum length

406 of the second abdominal pore; NPV: number of abdominal pores aligned vertically; NPH: number of abdominal  
 407 pores aligned horizontally; R1: maximum length of the second pore of the abdomen/H3; R2: number of  
 408 abdominal pores aligned vertically/H3; R3: number of abdominal pores aligned horizontally/W3.

409

410 Upon considering three morphogroups achieved by lumping *P. chalara* and *Podocyrtis* sp. cf.  
 411 *P. chalara*, the LDA ordination is highly similar to that obtained in the four-group analysis,  
 412 with all variation represented on the first two axes (~92.87 % on axis 1; **Figure S1**).  
 413 Classification results improved substantially, with  $94.5 \pm 3.1$  % of correctly identified  
 414 specimens in the three-group LDA (Table S2). Misclassification mainly occurred between *P.*  
 415 *goetheana* and *Podocyrtis* sp. cf. *P. goetheana*, occasionally also between *P. chalara* and  
 416 *Podocyrtis* sp. cf. *P. goetheana*, but never between *P. chalara* and *P. goetheana*.

417 **Table 4.** Average confusion matrix of the *Podocyrtis* morphotypes based on linear discriminant analysis (LDA)  
 418 performed on the matrix of our 13 morphometric variables (.i.e., measurements, pore counts and ratios).

**LDA results 4-group scenario**

	P_sp_cf_P_cha_&_P_sp_cf_P_goe	P_cha_&P_sp_cf_P_cha	P_cha_&P_sp_cf_P_goe	P_goe_&P_sp_cf_P_cha	P_goe_&P_sp_cf_P_goe	P_goe_&P_cha	total_c orrect
res_							<b>0.7351</b>
mea	0.011162791	0.204651163	0.001627907	0	0.04744186	0	<b>16279</b>
n							<b>0.0612</b>
res_s	0.013819733	0.059589621	0.005963544	0	0.024717954	0	<b>97375</b>
d							

419

420

421 **4.2. Artificial neural networks**

422 **4.2.1. Classification using the four morphogroups**

423 First, we trained neural networks on the dataset of 428 images attributed to the four  
 424 morphogroups (**Table 2** 4\_classes dataset) using a CNN with a VGG16 architecture. Prior to  
 425 the training and testing phases, images were manually grouped into four distinct classes (one

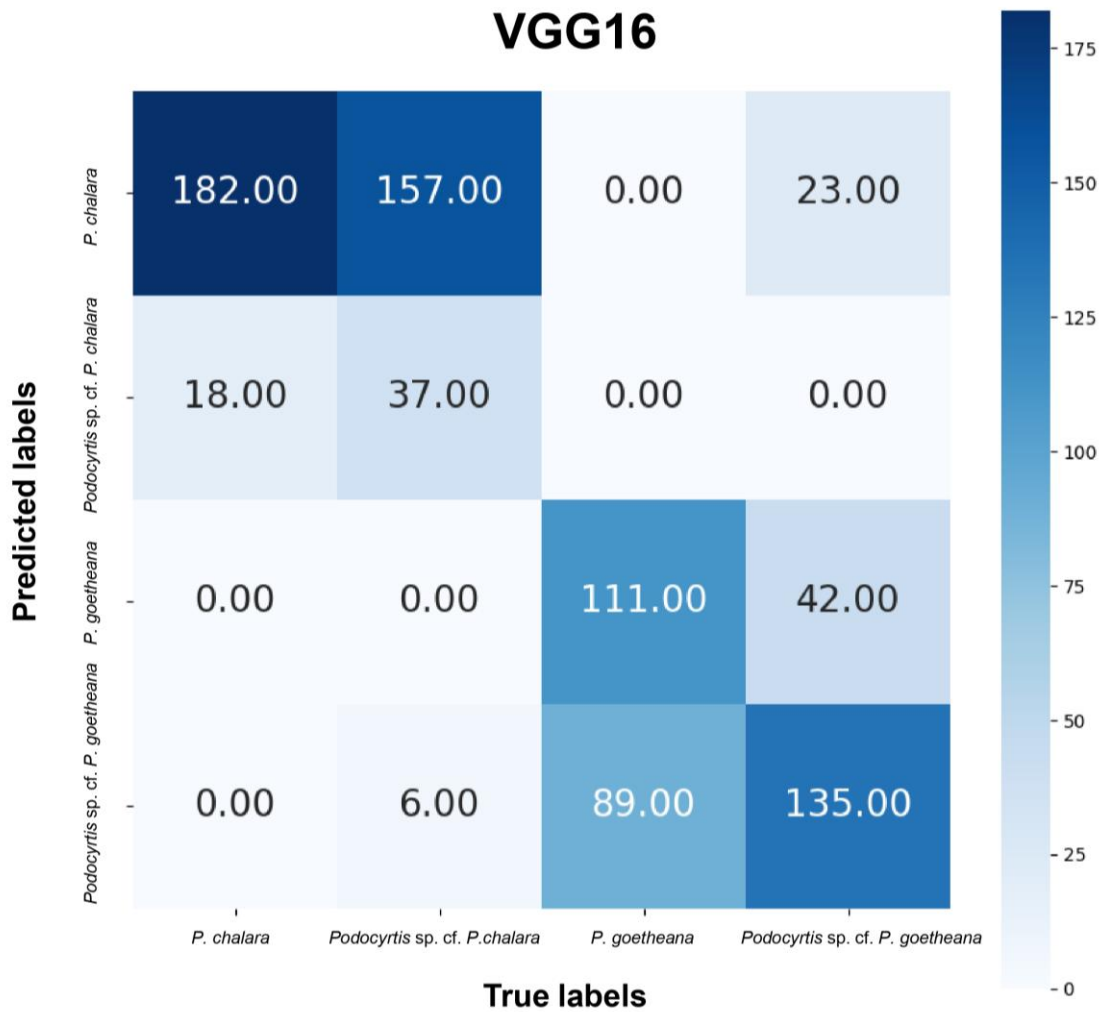
426 class per morphogroup). The analysis was run ten times with the pre-processing parameters  
 427 outlined in **Table 5**, which resulted to an identification accuracy of  $54.4 \pm 1.7$  % (**Figure**  
 428 **3**). These results indicate that, although the network was able to partially identify the  
 429 differences between the general morphologies of *P. chalara* + *Podocyrtis* sp. cf. *P. chalara*  
 430 versus those of *P. goetheana* + *Podocyrtis* sp. cf. *P. goetheana*, it was not able to accurately  
 431 distinguish all four morphogroups from each other.

432

433 **Table 5.** Summary of the tests performed on the 4\_classes and 3\_classes datasets using VGG16, STDP-based  
 434 SNN and SuperSpike-based SNN. Accuracy values are averaged from the results of the respective 10 test runs  
 435 and indicated as the mean  $\pm$  one standard deviation.

Dataset	Architecture	Test runs	Number of Epochs	Data pre-processing	Simulation time h:m:s	Accuracy (%) $\pm$ std mean $\pm$ std
4_classes	VGG16	10	20	Image resize to (224, 224) px	0:31:46	$54.40 \pm 1.74$
	VGG16	10	20	Image resize to (224, 224) px	0:17:37	$92.60 \pm 0.77$
3_classes	STDP-Network	10	100	Image resize to (128, 128) px & On-Off filter	0:05:4343	$90.40 \pm 0.4949$
	SuperSpike-Network	10	20	Image resize to (128, 128) px	0:23:26	$84.42 \pm 1.36$

436



437

438 **Figure 3.** Example of a confusion matrix obtained from random single run – Analysis of 4\_classes dataset with  
 439 VGG16. Correct assignments were reached in 54.40 % of the cases. The color scale indicates the number of  
 440 specimens.

441

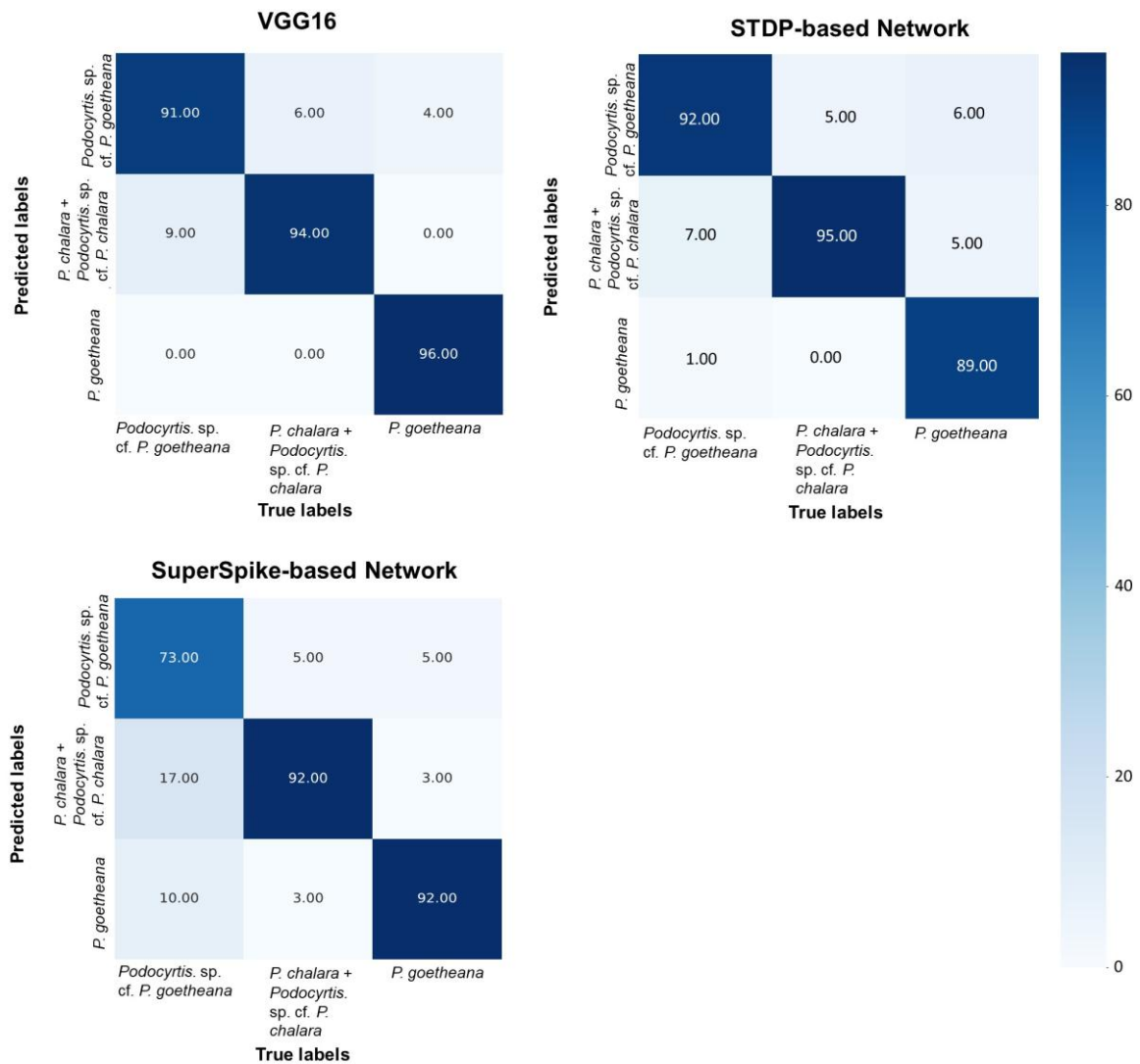
#### 442 **4.2.2. Classification using the three morphogroups supported by LDA**

443 Subsequently, we trained neural networks using a dataset with *a priori* assignment to  
 444 the three morphogroups that were recognized by LDA, i.e., *P. chalara* + *Podocyrtis* sp. cf. *P.*  
 445 *chalara* *Podocyrtis* sp. cf. *P. goetheana* and *P. goetheana*. For these analyses we compared  
 446 the performance of a VGG16 CNN, a STDP-based SNN and a SuperSpike-based SNN using  
 447 the 3\_classes dataset (**Table 3**). The resulting assignment results and average network



448 accuracies (**Figure 4**) indicate that, under our specified conditions, all neural networks are  
449 able to accurately assign specimens to their correct class when three predefined classes are  
450 used in combination with a large dataset of images. However, we observed substantial  
451 differences in the speed to conclude analyses; thus the STDP-based SNN was the fastest  
452 (around 6 minutes) due to the use of the local learning rule for training and one spike per  
453 image per neuron principale. Moreover, VGG16 came second with a time of around 17  
454 minutes due to the size of the network and the use of transfer learning and training of only the  
455 last layer. Last came the SuperSpike-based SNN with approximately 23 minutes per run  
456 because all layers of the network were trained from scratch during the training phase at the  
457 start of each run using a global learning rule.

458



459

460 **Figure 4.** Examples of confusion matrices obtained from random single runs – Analyses of 3\_classes dataset  
 461 with VGG16, STDP-based SNN and SuperSpike-based SNN. Correct assignments were reached in 92.60 %,   
 462 90.40 % and 84.42 % of the cases in VGG16, STDP-based SNN and SuperSpike-based SNN, respectively. The   
 463 color scale indicates the number of specimens.

464

465

## 466 5. Discussion

467 In this study, we examined the morphological variability in Eocene *Podocyrtilis*  
468 belonging to the anagenetic sequence that starts with *P. chalara* and ends with *P. goetheana*.  
469 Specifically, we examined and compared the performance of two analytical approaches in  
470 assigning individuals to *a priori* defined morphogroups that were constructed from qualitative  
471 observations, i.e., *P. chalara*, *Podocyrtilis* sp. cf. *P. chalara*, *Podocyrtilis* cf. *P. goetheana* and  
472 *P. goetheana*. The first approach involved LDA based on morphometric data, whereas the  
473 second was a neural network approach based on automatic image recognition. Both methods  
474 gave very similar results, which indicates that both morphometrics and image analysis  
475 evaluated shape differences in a highly similar way, suggesting that the results obtained with  
476 these two different methods are robust.

477 Comparing LDA and neural network approaches, assignment performances were  
478 comparatively low when four morphogroups were considered in the morphological transition  
479 from *P. chalara* to *P. goetheana*. The scatterplot of the LDA (**Figure 2**), indicated a large  
480 morphospace overlap between *P. chalara* and *Podocyrtilis* sp. cf. *P. chalara*, revealing that the  
481 qualitatively observed ‘differences’ were either not sampled in our datasets or that these  
482 differences are part of a larger spectrum of morphological variation and not informative to  
483 distinguish morphogroups. Given the similarity of LDA and neural networks, based on  
484 different datasets, the second hypothesis is more likely; it appears that *P. chalara* and  
485 *Podocyrtilis* sp. cf. *P. chalara* represent a single highly variable morphogroup. Morphospace  
486 overlap is also observed in the LDA between *Podocyrtilis* sp. cf. *P. goetheana* and *P.*  
487 *goetheana*, but it is much more limited than between *P. chalara* and *Podocyrtilis* sp. cf. *P.*  
488 *chalara*. Finally, *Podocyrtilis* sp. cf. *P. goetheana* also overlaps with *P. chalara* and *Podocyrtilis*  
489 sp. cf. *P. chalara* in morphospace occupation, however this overlap is small. The analyses  
490 conducted with the machine learning approach on four morphogroups confirm the results of

491 LDA, as VGG16 had significant difficulties in differentiating specimens of *P. chalara* from  
492 *Podocyrtis* sp. cf. *P. chalara* and vice-versa using stacked and segmented images, when all  
493 four morphogroup classes were pre-defined. This was also the case for some specimens of  
494 *Podocyrtis* sp. cf. *P. goetheana* and *P. goetheana*, which all resulted in an inferior  
495 performance of VGG16 compared to that of the LDA for the scenario with four  
496 morphogroups, i.e.,  $54.4 \pm 1.7$  % versus  $73.5 \pm 6.1$  %, respectively.

497 When *P. chalara* and *Podocyrtis* sp. cf. *P. chalara* are lumped in the same morphogroup,  
498 resulting in a three-group configuration, assignment probabilities improved strongly both for  
499 LDA and neural networks. On average  $94.5 \pm 3.1$  % of assignments were correct with LDA,  
500 whereas  $92.6 \pm 0.8$  %,  $90.4 \pm 0.5$  % and  $84.4 \pm 1.4$  % of the assignments were correct for  
501 VGG16, STDP-based SNN and SuperSpike-based SNN, respectively. Neural networks,  
502 mainly our CNN can accurately and quickly, assign specimens to the three pre-defined classes  
503 using a large dataset. Whereas the CNN performed highly similarly to LDA, both SNNs we  
504 used here performed less well, as had been documented for other tasks before (Tavanaej et al.,  
505 2019). Runs with the STDP-based SNN ran to completion fastest and given that the accuracy  
506 was only slightly reduced compared to LDA and VGG16, this approach may be preferred for  
507 datasets that require a very long runtime with similar CNNs. The accuracy of the SuperSpike-  
508 based SNN was significantly reduced compared to all the other classification methods that we  
509 used. Further work is required to determine the cause of this underperformance, but the lower  
510 accuracy for the SuperSpikeSuperSpike-based SNN is possibly due to the network size, as we  
511 used only using eight layers in our case compared to 16 layers in VGG-16.

512 As for the performance evaluation of the neural network approach, it is noteworthy  
513 that images were obtained manually for the purpose of our study, but advances in image  
514 technology now allow that much of the image acquisition and preparation procedures  
515 (photographing, stacking and segmentation) to be automated by the use of automatic

516 microscopes and modification of the AutoRadio\_Segmenter plugin's code (Marchant et al.,  
517 2020; Tetard et al., 2020). Using these automated procedures would facilitate the scalability  
518 of the entire analysis with larger datasets. If such automated procedures were to be used,  
519 constructing image datasets may potentially become more time-efficient than the various  
520 procedures that are required to develop a morphometric dataset. Another advantage of using  
521 neural network is their quick run time (**Table 5.**), although both accuracy and run time would  
522 increase upon using larger image datasets. Furthermore, standardizing the rotation and  
523 orientation of specimens is essential in morphometric studies; however, this requirement can  
524 be relaxed for neural networks, as in our case re-rotating and re-orienting were used in the  
525 data augmentation process to enlarge input datasets.

526 In our study, we evaluated assignment accuracy of LDA and machine learning with  
527 neural networks based on *a priori* group assignments; however, in the future, it would be  
528 useful to examine morphological variation without considering such assignments, e.g., by  
529 using other ordination techniques and/or by using unsupervised machine learning techniques.  
530 These methods could help in attempts to evaluate whether the three retained morphogroups  
531 represent natural entities, although based on fossil evidence only such assessments are very  
532 difficult. We refrain from such analyses here, as we believe these would be best conducted  
533 with a larger set of material that ideally would cover the total geographic range and the total  
534 stratigraphic interval covered by *P. chalara*, *Podocyrtis* sp. cf. *P. goetheana* and *P.*  
535 *goetheana*.

536 Future work could also be focused on trying to evaluate the capacity of VGG16 to  
537 accurately differentiate between the *P. chalara* and *Podocyrtis* sp. cf. *P. chalara* specimens,  
538 with an altered set of images. Indeed, the weighted activation heatmap (Grad-CAM)  
539 (Servaraju et al., 2017) generated from the runs with the 3-class dataset showed that the  
540 analytical focus of the network was centered around the thoracic and abdominal walls of the

541 specimens (**Figure S22** in **Supplementary material**). One could try to develop a dataset  
542 including several unstacked and non-segmented images per specimen, each one with a focus  
543 on specific morphological features. This would allow some images to contain as much detail  
544 as possible on abdominal features, whereas others would focus on other regions (e.g. the  
545 thorax) and include blurred features of the outer walls and backside of the abdomen. We  
546 hypothesize that these manipulations could force the network to focus its recognition  
547 capabilities on a larger set of morphological features. If this hypothesis would be correct, it  
548 would also facilitate the data acquisition process by eliminating the need to stack and segment  
549 the images themselves. Alternatively, it is possible that providing more fragmented  
550 information to neural networks would hamper an efficient learning process, with negative  
551 consequences on the accuracy of the following predictions, somewhat similar to what we  
552 observed in the VGG16 evaluation based on the 4-class dataset.

553

## 554 **6. Conclusion**

555 The aim of our work was to study the morphological variability in the anagenetic sequence of  
556 *P. chalara* to *P. goetheana* and to evaluate the performance of recognizing and classifying  
557 four *a priori* identified morphogroups with various machine learning algorithms based on  
558 neural networks that use image data as direct input in comparison to linear discriminant  
559 analysis using morphometric data. Our results demonstrate that LDA and neural networks  
560 provide very similar outcomes, indicating robust performances. With both approaches we  
561 encountered difficulties distinguishing *P. chalara* and *Podocyrthis* sp. cf. *P. chalara*,  
562 suggesting that the qualitative basis on which these morphogroups were recognized is to be  
563 revised. For both approaches, assignment probabilities drastically increased for the scenario  
564 where three morphogroups were recognized, lumping *P. chalara* and *Podocyrthis* sp. cf. *P.*  
565 *chalara*, and thus retaining *P. chalara* + *Podocyrthis* sp. cf. *P. chalara*, *Podocyrthis* sp. cf. *P.*

566 *goetheana* and *P. goetheana*. Further studies with more comprehensive sampling are required  
567 to document the likelihood of *Podocyrtilis* sp. cf. *P. goetheana* representing a separate natural  
568 entity, which additionally has implications for the position of bioevent RP16. However, our  
569 results indicate that the morphometric data that we used for LDA samples the morphological  
570 variability in the anagenetic sequence of *P. chalara* to *P. goetheana* in a comprehensive way.  
571 Secondly, neural network approaches were able to correctly assign most specimens, and  
572 therewith to accurately distinguish the three morphogroups directly from specimen images.  
573 These results indicate that VGG16, STDP-based SNNs, and even SuperSpike-based SNNs are  
574 capable of recognizing morphological variation in images and thus of reliably distinguishing  
575 radiolarian morphogroups, which could facilitate identification and help with reaching more  
576 objective taxonomic decisions. Furthermore, neural network approaches can be combined  
577 with automated image acquisition and preparation procedures (photographing, stacking and  
578 segmentation) that enable the creation of much larger image databases in a time-efficient  
579 manner. Analyses based on neural network architecture could thus take a fraction of the time  
580 that would be required for a trained taxonomist/(paleo)biologist to create and analyze  
581 quantitative morphometric datasets. In conclusion, neural network approaches based on  
582 images of (paleo)biological specimens may provide promising opportunities to guide more  
583 objective taxonomic decisions.

584

### 585 **Data availability**

586 Microscopic slides are prepared and stored at UMR 8198 – Evo-Eco-Paleo of the University  
587 of Lille, France. The datasets (<https://doi.org/10.57745/8KBOFP>, Pinto et al. 2023) have been  
588 archived in the repository of the University of Lille at Recherche Data Gouv. The codes are  
589 available at

590 <https://archive.softwareheritage.org/browse/directory/cc7d8ef1505299a208adcde597a98d90b>

591 [0ca47d6/https://archive.softwareheritage.org/browse/directory/cc7d8ef1505299a208adcde597](https://archive.softwareheritage.org/browse/directory/cc7d8ef1505299a208adcde597a98d90b0ca47d6/)  
592 [a98d90b0ca47d6/](https://archive.softwareheritage.org/browse/directory/cc7d8ef1505299a208adcde597a98d90b0ca47d6/) (Elbez, 2023).

593

## 594 **Acknowledgments**

595 This study was partly funded by the French government through the program  
596 “Investissements d’avenir” (I-ULNE SITE/ANR-16-IDEX-0004 ULNE) managed by the  
597 National Research Agency. It also received funding from the European Union’s Horizon 2020  
598 research and innovation program under the Marie Skłodowska-Curie grant agreement no.  
599 847568. It was also supported by UMR 8198 Evo-Eco-Paléo and IRCICA (CNRS and Univ.  
600 Lille USR-3380).

601 A special thanks to Mazdak Fatahi for very helpful discussions regarding machine learning  
602 techniques and to Sylvie Regnier for help and advice with the sample preparation.

603

604

605

606

607

608

609

610

611



612 **References**

- 613 Balouek, D., Carpen Amarie, A., Charrier, G., Desprez, F., Jeannot, E., Jeanvoine, E., Lèbre,  
614 A., Margery, D., Niclausse, N., Nussbaum, L., Richard, O., Perez, C., Quesnel, F.,  
615 Rohr, C., & Sarzyniec, L., 2013, Adding virtualization capabilities to the Grid'5000  
616 testbed: In *Cloud Computing and Services Science, Communications in Computer and  
617 Information Science*). Springer International Publishing, v. 367, p. 3-20.
- 618 Beaufort, L., and Dollfus, D., 2004, Automatic recognition of coccoliths by dynamical neural  
619 networks: *Marine Micropaleontology*, v. 51, p. 57-73.  
620 doi:10.1016/j.marmicro.2003.09.003.
- 621 Bourel, B., Marchant, R., de Garidel-Thoron, T., Tetard, M., Barboni, D., Gally, Y., and  
622 Beaufort, L., 2020, Automated recognition by multiple convolutional neural networks  
623 of modern, fossil, intact and damaged pollen grains: *Computers and Geosciences*, v.  
624 140, 104498. doi:10.1016/j.cageo.2020.104498.
- 625 Brocher, J., 2022, biovoxxel/BioVoxxel-Toolbox: BioVoxxel Toolbox v2.5.3. Zenodo.  
626 doi:10.5281/zenodo.5986129.
- 627 Carlsson, V., Danelian, T., Boulet, P., Devienne, P., Laforge, A., and Renaudie, J., 2022,  
628 Artificial intelligence applied to the classification of eight middle Eocene species of  
629 the genus *Podocyrthis* (polycystine radiolaria): *Journal of Micropalaeontology*, v. 41, p.  
630 165–182.
- 631 Cortes, C., and Vapnik, V., 1995, Support-vector networks: *Machine Learning*, v. 20, p. 273–  
632 297.
- 633 Danelian, T., and Johnson, K.G., 2001, Patterns of biotic change in Middle Jurassic to Early  
634 Cretaceous Tethyan radiolarian: *Marine Micropaleontology*, v. 43, p. 239-260.  
635 doi:10.1016/S0377-8398(01)00029-9.

636 Danelian, T., and Macleod, N., 2019, Morphometric Analysis of Two Eocene Related  
637 Radiolarian Species of the Podocyrtilis (Lampterium) Lineage: Paleontological  
638 Research, v. 23, p. 314–330.

639 Danelian, T., Zambetakis-Lekkas, A., Galoyan, G., Sosson, M., Asatryan, G., Hubert, B., and  
640 Grigoryan, A., 2014, Reconstructing Upper Cretaceous (Cenomanian)  
641 paleoenvironments in Armenia based on Radiolaria and benthic Foraminifera;  
642 implications for the geodynamic evolution of the Tethyan realm in the Lesser  
643 Caucasus: Palaeogeography, Palaeoclimatology, Palaeoecology, v. 413, p. 123–132.

644 Danelian, T., Baudin, F., Gardin, S., Masure, E., Ricordel, C., Fili, I., Meçaj, T., and Muska,  
645 K., 2007, The record of mid Cretaceous oceanic anoxic events from the Ionian zone of  
646 southern Albania: Revue de Micropaléontologie, v. 50, p. 225–237.

647 Danelian, T., Le Callonec, L., Erbacher, J., Mosher, D.C., Malone, M.J., Berti, D., Bice, K.L.,  
648 Bostock, H., Brumsack, H.-J., Forster, A., Heidersdorf, F., Henderiks, J., Janecek, T.J.,  
649 Junium, C., Macleod, K., Meyers, P.A., Mutterlose, J.H., Nishi, H., Norris, R.D., Ogg,  
650 J.G., O'Regan, M.A., Rea, B., Sexton, P., Sturt-Fredricks, H., Suganuma, Y., Thurow,  
651 J.W., Wilson, P.A., Wise, S.W., and Glatz, C., 2005, Preliminary results on  
652 Cretaceous-Tertiary tropical Atlantic pelagic sedimentation (Demerara Rise, ODP Leg  
653 207): Comptes Rendus Geoscience, v. 337, p. 609–616.

654 Dollfus, D., and Beaufort, L., 1999, Fat neural network for recognition of position-normalized  
655 objects. Neural Networks, v.12, p. 553-560. doi:10.1016/S0893-6080(99)00011-8.

656 [code] Elbez, H., 2023, Code for: Morphometrics and machine learning discrimination of the  
657 middle Eocene radiolarian species *Podocyrtilis chalara*, *P. goetheana* and their  
658 morphological intermediates, deposited at  
659 [https://archive.softwareheritage.org/browse/directory/cc7d8ef1505299a208adcde597a](https://archive.softwareheritage.org/browse/directory/cc7d8ef1505299a208adcde597a98d90b0ca47d6/)  
660 [98d90b0ca47d6/](https://archive.softwareheritage.org/browse/directory/cc7d8ef1505299a208adcde597a98d90b0ca47d6/) 2023-08-24.

661 Haeckel, E., 1887, Report on the Radiolaria collected by H.M.S. Challenger during the years  
662 1873-1876. Report on the Scientific Results of the Voyage of H.M.S. Challenger  
663 during the years 1873-1876. 18: 1-1803.

664 Falez, P., 2019, Improving Spiking Neural Networks Trained with Spike Timing Dependent  
665 Plasticity for Image Recognition [phdthesis]: Université de Lille.

666 Hijazi, S., Kumar, R., and Rowen, C., 2015, Using Convolutional Neural Networks for Image  
667 Recognition: Cadence, Cadence Design Systems Inc., p. 1–12.

668 Hsiang, A.Y., Brombacher, A., Rillo, M.C., Mleneck-Vautravers, M.J., Conn, S., Lordsmith,  
669 S., Jentzen, A., Henehan, M.J., Metcalfe, B., Fenton, I.S., Wade, B.S., Fox, L.,  
670 Meilland, J., Davis, C. V., Baranowski, U., Groeneveld, J., Edgar, K.M., Movellan,  
671 A., Aze, T., Dowsett, H. J., Giles Miller, C., Rios, N., and Hull, P. M., 2019, Endless  
672 Forams: >34,000 modern planktonic foraminiferal images for taxonomic training and  
673 automated species recognition using convolutional neural networks: *Paleoceanography*  
674 and *Paleoclimatology*, 34, 1157-1177. doi:10.1029/2019PA003612.

675 Itaki, T., Taira, Y., Kuwamori, N., Saito, H., Ikehara, M., and Hoshino, T., 2020, Innovative  
676 microfossil (radiolarian) analysis using a system for automated image collection and  
677 AI-based classification of species: *Scientific Reports*. doi:10.1038/s41598-020-77812-  
678 6.

679 Lever, J., Krzywinski, M., and Altman, N., 2017, Principal component analysis: *Nature*  
680 *Methods*, v. 14, p. 641–642.

681 Maass, W., 1997, Networks of spiking neurons: The third generation of neural network  
682 models: *Neural Networks*, v. 10, p. 1659–1671.

683 Marchant, R., Tetard, M., Pratiwi, A., Adebayo, M., and de Garidel-Thoron, T., 2020,  
684 Automated analysis of foraminifera fossil records by image classification using a  
685 convolutional neural network: *Journal of Micropalaeontology*, v. 39, p. 183–202.

686 Masquelier, T., and Thorpe, S.J., 2007, Unsupervised Learning of Visual Features through  
687 Spike Timing Dependent Plasticity: *PLOS Computational Biology*, v. 3, p. e31.

688 Meunier, M., and Danelian, T., 2022, Astronomical calibration of late middle Eocene  
689 radiolarian bioevents from ODP Site 1260 (equatorial Atlantic, Leg 207) and  
690 refinement of the global tropical radiolarian biozonation: *Journal of*  
691 *Micropalaeontology*, v. 41, p. 1–27.

692 Meunier, M., and Danelian, T., 2023, Progress in understanding middle Eocene nassellarian  
693 (Radiolaria, Polycystinea) diversity; new insights from the western equatorial Atlantic  
694 Ocean: *Journal of Paleontology*, v. 97, p. 1–25.

695 Mitra, R., Marchitto, T.M., Ge, Q., Zhong, B., Kanakiya, B., Cook, M.S., Fehrenbacher, J.S.,  
696 Ortiz, J.D., Tripathi, A., and Lobaton, E., 2019, Automated species-level identification  
697 of planktic foraminifera using convolutional neural networks, with comparison to  
698 human performance: *Marine Micropaleontology*, v. 148, p. 1-14.  
699 doi:10.1016/j.marmicro.2019.01.005.

700 Moore, T.C., 1972, Mid-Tertiary Evolution of the Radiolarian Genus *Calocycletta*:  
701 *Micropaleontology*, v. 18, p. 144–152.

702 Nigrini, C.A., Sanfilippo, A., and Moore, T.J., 2005, Radiolarian biostratigraphy and  
703 chronology of radiolarian events of ODP Leg 199 sites and EW9709 sediment cores:  
704 Supplement to: Nigrini, CA et al. (2005): Cenozoic Radiolarian Biostratigraphy: A  
705 Magnetobiostratigraphic Chronology of Cenozoic Sequences from ODP Sites 1218,  
706 1219, and 1220, Equatorial Pacific. In: Wilson, PA; Lyle, M; Firth, JV (Eds.)  
707 Proceedings of the Ocean Drilling Program, Scientific Results, College Station, TX  
708 (Ocean Drilling Program), v. 199, p. 1-76,  
709 <https://doi.org/10.2973/Odp.Proc.Sr.199.225.2005>.

710 Obut, O., and Iwata, K., 2000, Lower Cambrian Radiolaria from the Gorny Altai (southern  
711 West Siberia): Journal of Geology and Geophysics, v. 41.

712 Oksanen, J., Blanchet, F.G., Kindt, R., Legendre, P., Minchin, P.R., O'hara, R.B., Simpson,  
713 G.L., Solymos, P., Stevenes, M.H.H., Wagner, H., 2013, Package 'vegan': Community  
714 ecology package, v. 2, p. 1–295.

715 Paszke, A., Gross, S., Massa, F., Lerer, A., Bradbury, J., Chanan, G., Killeen, T., Lin, Z.,  
716 Gimelshein, N., Antiga, L., Desmaison, A., Kopf, A., Yang, E., DeVito, Z., Raison,  
717 M., Tejani, A., Chilamkurthy, S., Steiner, B., Fang, L., Bai, J., and Chintala, S., 2019,  
718 PyTorch: An Imperative Style, High-Performance Deep Learning Library: 33<sup>rd</sup>  
719 NeurIPS, Vancouver, British Columbia, Canada, <https://arxiv.org/abs/1912.01703>

720 Pehle, C.-G., and Pedersen, J.E., 2021, Norse - A deep learning library for spiking neural  
721 networks (0.0.5), Zenodo, <https://doi.org/10.5281/zenodo.4422025>.

722 Pinto, F., Carlsson, V., Meunier, M., Van Bocxlaer., B., Elbez, H., Cueille, M., Boulet, P and  
723 Danelian, T, 2023, Data for the: Morphometrics and machine learning discrimination  
724 of the middle Eocene radiolarian species *Podocyrstis chalara*, *P. goetheana* and their  
725 morphological intermediates, Recherche Data Gouv,  
726 <https://doi.org/10.57745/8KBOFP>.

727 Pouille, L., Obut, O., Danelian, T., and Sennikov, N., 2011, Lower Cambrian (Botomian)  
728 polycystine Radiolaria from the Altai Mountains (southern Siberia, Russia): Comptes  
729 Rendus Palevol, v. 10, p. 627–633.

730 R Core Team, 2022, R: a language and environment for statistical computing: R Foundation  
731 for Statistical Computing. <https://www.R-project.org>.

732 Renaudie, J., Danelian, T., Saint Martin, S., Le Callonnec, L., and Tribovillard, N., 2010,  
733 Siliceous phytoplankton response to a Middle Eocene warming event recorded in the

734 tropical Atlantic (Demerara Rise, ODP Site 1260A): *Palaeogeography,*  
735 *Palaeoclimatology, Palaeoecology*, v. 286, p. 121–134.

736 Renaudie, J., Lazarus, D., 2013, On the accuracy of paleodiversity reconstructions: a case  
737 study in Antarctic Neogene radiolarians: *Paleobiology*, v. 39(3), p. 491-509.

738 Renaudie, J., Gray, R., and Lazarus, D.B., 2018, Accuracy of a neural net classification of  
739 closely-related species of microfossils from a sparse dataset of unedited images. *PeerJ*  
740 *Preprints*, 6:e27328v1.

741 Riedel, R.W., 1971, Cenozoic Radiolaria from the western tropical Pacific, Leg 7.: *Init. Repts.*  
742 *DSDP*, v. 7, p. 1592–1627.

743 Riedel, W.R., and Sanfilippo, A., 1978, Stratigraphy and Evolution of Tropical Cenozoic  
744 Radiolarians: *Micropaleontology*, v. 24, p. 61–96.

745 Ripley, B., Venables, B., Bates, D.M., Hornik, K., Gebhardt, A., Firth, D., Ripley, M.B.,  
746 2013, Package ‘mass’: *Cran r*, 538, p. 113–120.

747 Rohlf, F., and Bookstein, F., 1991, Size and Shape (Book Reviews: Proceedings of the  
748 Michigan Morphometrics Workshop.): *Science*, v. 253, p. 345-362.

749 Sanfilippo, A., and Riedel, W.R., 1970, Post-Eocene “Closed” Theoperid Radiolarians:  
750 *Micropaleontology*, v. 16, p. 446–462.

751 Sanfilippo, A., and Riedel, W.R., 1992, The Origin and Evolution of Pterocorythidae  
752 (Radiolaria): A Cenozoic Phylogenetic Study: *Micropaleontology*, v. 38, p. 1.

753 Sanfilippo, A., and Nigrini, C., 1998, Code numbers for Cenozoic low latitude radiolarian  
754 biostratigraphic zones and GPTS conversion tables: *Marine Micropaleontology*, v. 33,  
755 p. 109–156.

756 Schneider, C.A., Rasband, W.S., and Eliceiri, K.W., 2012, NIH Image to ImageJ: 25 years of  
757 image analysis: *Nature Methods*, v. 9, p. 671–675.

758 Simonyan, K., and Zisserman, A., 2015, Very Deep Convolutional Networks for Large-Scale  
759 Image Recognition: ICLR, San Diego, California, USA,  
760 <https://arxiv.org/abs/1409.1556>.

761 Tavanaei, A., Ghodrati, M., Kheradpisheh, S. R., Masquelier, T., & Maida, A., 2019, Deep  
762 learning in spiking neural networks, *Neural Networks*, v. 111, p. 47-63,  
763 doi:10.1016/j.neunet.2018.12.002.

764 Tetard, M., Monnet, C., Noble, P., and Danelian T., 2017, Biodiversity patterns of Silurian  
765 Radiolaria: *Earth-Science Reviews*, v.173, p. 77-83.

766 Tetard, M., Marchant, R., Cortese, G., Gally, Y., de Garidel-Thoron, T., and Beaufort, L.,  
767 2020, Technical note: A new automated radiolarian image acquisition, stacking,  
768 processing, segmentation and identification workflow: *Climate of the Past*, v. 16, p.  
769 2415–2429.

770 Venables, W.N., and Ripley, B.D., 2002, Random and Mixed Effects, *in* Venables, W.N. and  
771 Ripley, B.D., eds., *Modern Applied Statistics with S*, Statistics and Computing: New  
772 York, NY, Springer, p. 271–300.

773 Watanabe, M., Kawagata, S., Aita, Y., Suzuki, N., and Kamikuri, S., 2022, Changes in  
774 morphological parameters of the radiolarian *Lampterium* lineage from the middle  
775 Eocene in the tropical Pacific: *Marine Micropaleontology*, v. 173, 102125.

776 Westerhold, T., and Röhl, U., 2013, Orbital pacing of Eocene climate during the Middle  
777 Eocene Climate Optimum and the chron C19r event: Missing link found in the tropical  
778 western Atlantic: *Orbital Pacing of Eocene Climate: Geochemistry, Geophysics,*  
779 *Geosystems*, v. 14, p. 4811–4825.

780 Yang, Z.R., and Yang, Z., 2014, Artificial Neural Networks, *Comprehensive Biomedical*  
781 *Physics: Elsevier*, p. 1–17.

782 Zenke, F., and Ganguli, S., 2018, SuperSpike: Supervised Learning in Multilayer Spiking  
783 Neural Networks: Neural Computation, v. 30, p. 1514–1541